Applied Surface Science 608 (2023) 155233

Contents lists available at ScienceDirect

Applied Surface Science

journal homepage: www.elsevier.com/locate/apsusc

Full Length Article

Impact of interfacial engineering on MgO-based resistive switching devices for low-power applications

Samuel Chen Wai Chow [a,b], Putu Andhita Dananjaya [a], Jia Min Ang [a,b], Desmond Jia Jun Loy [b], Jia Rui Thong [a,b], Siew Wei Hoo [a], Eng Huat Toh [b], Wen Siang Lew [a,*]

[a] School of Physical and Mathematical Sciences, Nanyang Technological University 21 Nanyang Link, Singapore 637371, Singapore
[b] GLOBALFOUNDRIES Singapore Pte Ltd, 60 Woodlands Industrial Park D Street 2, Singapore 738406, Singapore

ARTICLE INFO

Keywords:
Filament evolution
Interface engineering
Oxygen vacancy
Bilayer
Conduction mechanism
Resistive switching

ABSTRACT

In this work, the resistive switching characteristics of MgO/Al_2O_3-based resistive random-access memory (ReRAM) devices have been reported. Analysis shows the change in dominant conduction mechanism from space-charge-limited conduction to Schottky emission owing to the incorporation of an Al_2O_3 insertion layer. The MgO/Al_2O_3 bilayer ReRAM devices exhibit lower power operation (50.6% reduction) and better switching uniformity as compared to single-layer devices, depending on the stack configuration. This can be attributed to the lower oxygen vacancy accumulation and filament confinement at the MgO/Al_2O_3 interface, resulting in a more controllable switching operation. Further X-ray photoelectron spectroscopy (XPS) depth profile analysis of the bilayer device reveals that the switching dynamics are correlated directly with the oxygen vacancy concentrations. These findings indicate the importance of interfacial layer engineering in improving the resistive switching properties of MgO-based memory devices, thus allowing for low-power applications.

1. Introduction

Resistive random-access memory (ReRAM) based on metal oxides such as TiO_2, Ta_2O_5, HfO_2, ZrO_2, etc., has attracted interest owing to its potential in terms of scalability, read latency, write performance, cost-*per*-bit, and complementary metal–oxidesemiconductor (CMOS) architecture compatibility [1–6]. Nevertheless, there are still concerns regarding device variability, power consumption for embedded applications, read and write disturbance in crossbar array integration that hinder ReRAM commercialization [7–11]. Among these metal oxides, HfO_2 and Ta_2O_5 have been widely investigated due to their resistive performance and mature process technology [5,12]. Comparably, extensive investigations on magnetic tunnel junctions (MTJs) using MgO as a barrier layer have made significant advances in process technologies, indicating its industrial compatibility [13]. Moreover, MgO has been reported to exhibit resistive switching properties and is a potential candidate for ReRAM applications [14–17].

MgO has a wide band gap (7.3–7.8 eV) to ensure sufficient band offsets, moderate dielectric constant (9.8–10), high thermal stability, and high breakdown field (up to 12 MV cm^{-1}) [18–21]. Recently, MgO-based ReRAM devices have seen success in terms of ultra-low operation voltages (~0.22 V), self-current limiting characteristics, and biodegradable transient ReRAM applications [9,16,22]. Therefore, the use of MgO as a switching layer (SL) can potentially address certain concerns of current ReRAM devices. Additionally, studies have indicated the beneficial effects of an Al_2O_3 insertion layer on overall ReRAM device performance due to dielectric properties such as a wider band gap (8.8 eV) and Al-O bond energy [23–26]. Thus far, asymmetric conductive filament formations in bilayer and tri-layer stack configurations have been attributed to the presence of Al_2O_3, allowing for more control on the switching location across the filament [7,27]. However, investigations on the resistive switching behaviour and current conduction mechanisms in bilayer MgO/Al_2O_3-based ReRAM is currently lacking in literature.

In this study, the resistive switching of single-layer MgO and bilayer MgO/Al_2O_3-based ReRAM stacks were investigated. Here, the low-power characteristics and lower high resistance state variation of the bilayer device was observed. The I-V characterization results also show that the dominant conduction mechanism in the single-layer MgO device is space-charge-limited conduction (SCLC) but can either be SCLC or Schottky emission (SE) in the bilayer MgO/Al_2O_3-based device depending on the stacking order. Through the SE investigations, the

* Corresponding author.
E-mail address: wensiang@ntu.edu.sg (W.S. Lew).

https://doi.org/10.1016/j.apsusc.2022.155233
Received 6 July 2022; Received in revised form 3 October 2022; Accepted 5 October 2022
Available online 8 October 2022

Schottky barrier heights of both the top and bottom interfaces were extracted through the SE linear fits. Additionally, XPS depth profile analysis was performed to support the proposed switching model, and an explanation on the resistive switching behaviour of the bilayer memory device was provided.

2. Method

In this work, the ReRAM devices with effective areas of 5 × 5 μm^2 to 50 × 50 μm^2 were fabricated. Starting with a clean Si/SiO_2 wafer, the bottom electrode (BE) was patterned via UV lithography and a 11 nm trench was etched by ion milling. Following the 1 nm Ti adhesion layer deposition, the 10 nm Pt BE was deposited via magnetron sputtering. Atomic force microscopy (AFM, Park NX10, Park Systems) in non-contact mode was used to investigate the surface roughness of the embedded BE. This was followed by top electrode (TE) patterning, and thin SL and 30 nm Ti TE deposition. The switching layers were deposited via RF magnetron sputtering (ATC-Orion 8 UHV, AJA International) with MgO and Al_2O_3 sputtering targets. The 3D, cross-sectional view, and scanning electron microscopy (SEM) top-view of the device structure was illustrated in Fig. 1**a - c**, respectively. The SL of interest in this work consist of 5 nm MgO (P-M-T), 5 nm Al_2O_3 (P-A-T), 4 nm MgO/1 nm Al_2O_3 (P-M-A-T), and 1 nm Al_2O_3/4 nm MgO (P-A-M-T). Fig. 1**d - g** shows the transmission electron microscopy (TEM) cross-sectional view of P-M-T, P-A-T, P-M-A-T, and P-A-M-T, respectively. The corresponding energy-dispersive X-ray spectroscopy (EDX) line scan analysis was shown in Fig. 1**h - k**. General I-V measurements were characterized using the Keysight B1500A semiconductor device parameter analyzer, while *in-situ* temperature I-V measurements were characterized using the Keithley 4200A-SCS parameter analyzer. All measurements were conducted by applying voltage on the TE while keeping the BE grounded. In addition, a compliance current (CC) of 200 μA was provided during the forming and set cycles. Annealing of the pristine devices were performed in high vacuum conditions at various temperatures for 30 min each time. Finally, the depth profile analyses of the composition and chemical states of the P-M-T and P-A-M-T samples were performed via XPS (Axis Supra, Kratos Analytical).

3. Results and discussion

Fig. 2**a** shows the typical forming I-V curve of the various stack configurations with CC of 200 μA to avoid a hard breakdown on the 1R structure. The forming voltage of P-M-T is clearly lower than P-A-T. On the other hand, the bilayer P-M-A-T and P-A-M-T stacks results in a further increase in forming voltage. In Fig. 2**b**, the cumulative probability plot of the forming voltage of 5 devices from each stack demonstrates the low pristine device to device variability.

Following the forming cycle, the devices went through 20 consecutive set/reset cycles as shown in Fig. 2**c - f**. The high/low resistance state (HRS/LRS) values read at 0.2 V and set/reset voltages extracted from 5 devices × 20 cycles of each stack were compiled into the box plots shown in Fig. 2**g** and **h**, respectively. Consistently, an increase in HRS/LRS values of the P-A-M-T stack were observed with averages of ~535 kΩ/~33 kΩ (HRS/LRS) which are much higher than ~198 kΩ/~19 kΩ, ~130 kΩ/~16 kΩ, and ~199 kΩ/~24 kΩ of P-M-T, P-A-T, and P-M-A-T, respectively. Furthermore, the coefficients of variation of HRS have shown improvements from 25.8 % of single-layer P-M-T to 12.5 % of bilayer P-A-M-T, while there were no significant differences between the LRS of P-M-T (27.4 %) and P-A-M-T (27.3 %). To the contrary, bilayer P-M-A-T exhibited larger variations of 42.5 % and 50.7 % for HRS and LRS, respectively. This implies that the bilayer stacking order plays a vital role in the switching and conduction mechanism of the device.

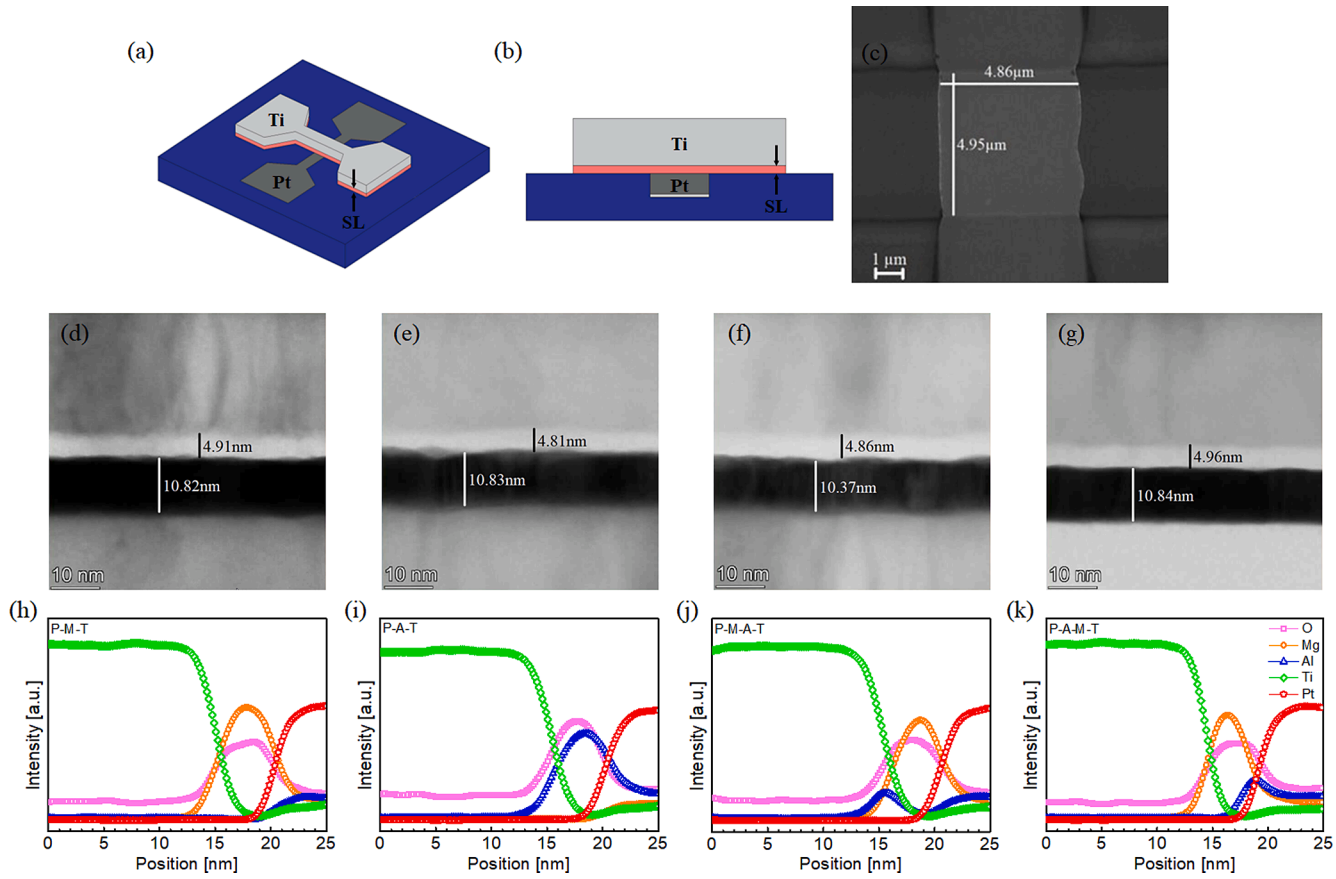

Fig. 1. Schematics of fabricated ReRAM devices: (a) 3D view and (b) Cross-sectional view. (c) SEM top-view with device area of 4.95 × 4.86 μm^2. (d - g) TEM cross-sectional view and (h - k) EDX line scan analysis of P-M-T, P-A-T, P-M-A-T, and P-A-M-T, respectively.

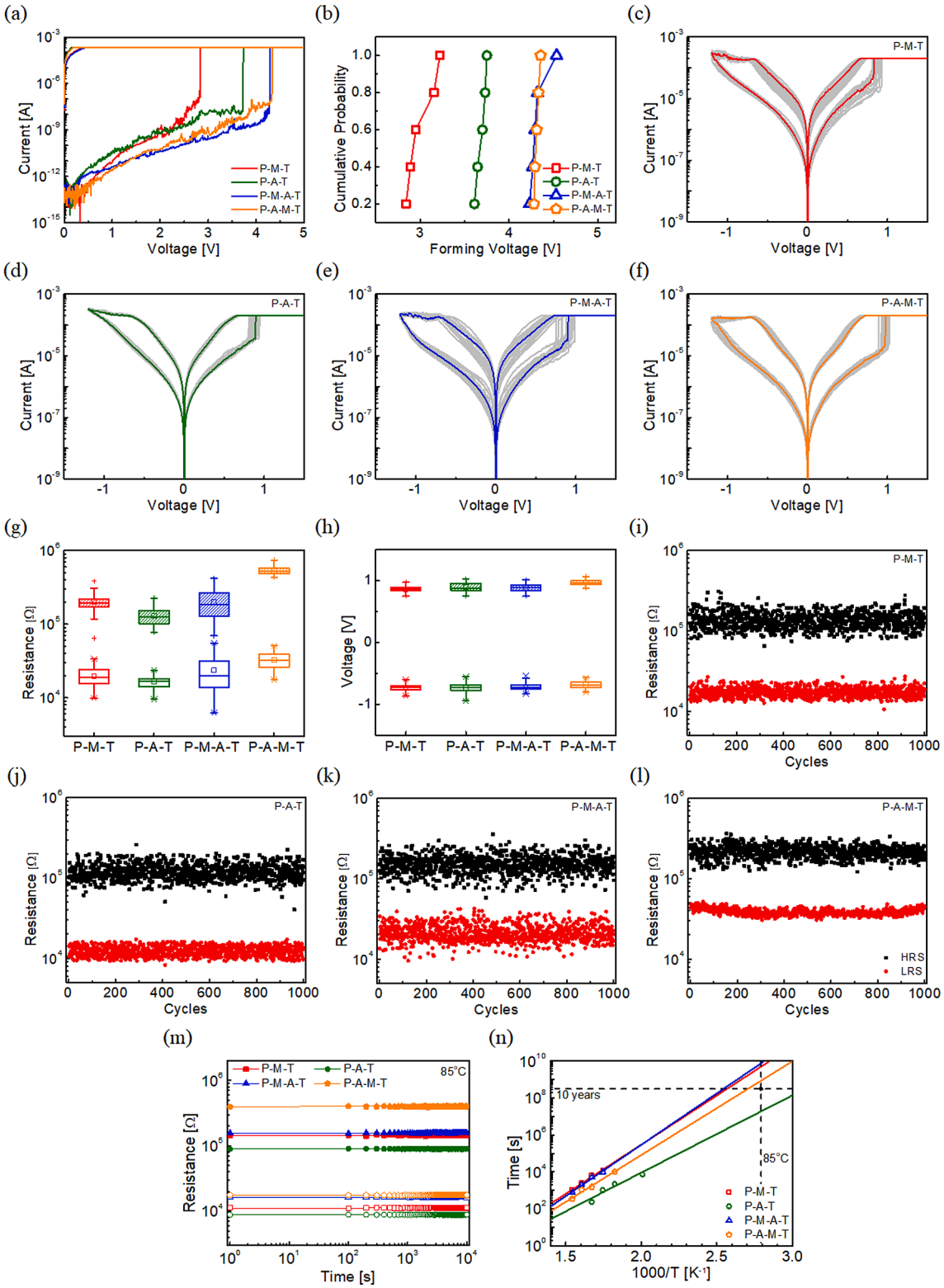

Fig. 2. P-M-T, P-A-T, P-M-A-T, and P-A-M-T forming (a) I-V characteristics and (b) statistical distributions (5 devices from each stack). 20 consecutive I-V cycles of the (c) P-M-T, (d) P-A-T, (e) P-M-A-T, and (f) P-A-M-T device after forming. Statistical distributions of (g) HRS/LRS values (pattern/plain) extracted at 0.2 V and (h) set/reset voltages (pattern/plain) from 5 devices × 20 cycles of each stack. (i - l) Distribution of HRS/LRS values (square/circle) from AC measurements using V_{set} = 1.5 V and V_{reset} = -1.7 V, 200 ns pulses on the 1R P-M-T, P-A-T, P-M-A-T, and P-A-M-T device, respectively for 1,000 cycles. (m) Memory retention of HRS/LRS (solid/hollow) for 10^4 s at V_{read} = 0.2 V. (n) Temperature-dependent retention characteristics of the various stacks. Devices were subjected to *in-situ* temperature stress with V_{read} = 0.05 V and the results were extrapolated to 85 °C.

Meanwhile, the P-A-M-T stack generally exhibited slightly higher set voltage of 0.97 V but lower reset voltage of −0.68 V among those investigated. The coefficients of variation of the set and reset voltages remained low at 4.5 % and 8.8 %, respectively. The maximum operating powers of 20 cycles that can be observed from the reset cycles of each stack were estimated to be ~443 μW, ~410 μW, ~290 μW, and ~219 μW for P-M-T, P-A-T, P-M-A-T, and P-A-M-T, respectively. Thus, there was a 50.6 % reduction in operating power from single-layer P-M-T to bilayer P-A-M-T. Subsequently, AC measurements were conducted (no external current limiter) on the 1R devices (Fig. 2**i - l**) using 200 ns pulses with 1.5 V and −1.7 V for V_{set} and V_{reset}, respectively for at least 1,000 cycles [28]. The reading voltage V_{read} was 0.2 V, and no significant degradations were observed during the measurements.

Fig. 2**m** plots the memory retention of HRS/LRS for the various stacks up to 10^4 s at 85 °C. No noticeable degradations were observed within this period and further temperature-dependent retention characteristics of the devices were investigated using *in-situ* temperature stress [29–32]. The times to failure with respect to varying temperatures were plotted and extrapolated following the Arrhenius equation. Fig. 2**n** shows that there were no issues with retention of P-M-T, P-M-A-T, and P-A-M-T as the devices demonstrated more than 10 years at 85 °C. However, this was not observed for the P-A-T device, which could suggest state instability of the Al_2O_3 SL. With the addition of Al_2O_3, both P-M-A-T and P-A-M-T were able to demonstrates memory retention over 10 years at 85 °C (Fig. 2**n**). However, there was a noticeable decrease in the retention properties for P-A-M-T which could suggest more significant changes in the redox reaction mechanism as compared to P-M-A-T [32]. In the absence of an electric field, the activation energy (E_a) of the redox reactions in the device was obtained from the Arrhenius equation that can be expressed in Eq. (1) [30,31]:

$$t_{failure} = Ae^{\frac{E_a}{k_B T}} \quad (1)$$

Where $t_{failure}$ is the time to failure, A is the pre-exponential factor, E_a is the activation energy, k_B is the Boltzmann constant, and T is the absolute temperature. The activation energy values were extracted from the P-M-T (1.07 eV), P-A-T (0.83 eV), P-M-A-T (1.11 eV), and P-A-M-T (0.99 eV) devices. The values from P-M-T and P-M-A-T were similar, while a larger change in activation energy was observed from P-A-M-T due to the incorporation of Al_2O_3 towards the Pt BE. Thus, it is believed that the Al_2O_3 layer in this configuration could result in accelerated degradation of the retention properties. Nevertheless, the P-A-M-T device was able to demonstrate good memory retention.

Fig. 3 plots the transient response current waveform with of a 200 ns pulse width with rise and fall time of 20 ns for the various devices. The peak powers of the set/reset measurements were calculated to be ~1283 μW/~1376 μW, ~1876 μW/~1859 μW, ~1691 μW/~1722 μW, and ~805 μW/~759 μW for P-M-T, P-A-T, P-M-A-T, and P-A-M-T, respectively. Thus, similar to the DC characteristics, a reduction in power can be observed in the P-A-M-T stack. The energy consumption can be obtained by the time-integral of power [33]. The P-A-M-T device exhibited lower energy consumption with ~134 pJ/~128 pJ as compared to ~226 pJ/~235 pJ (P-M-T), ~355 pJ/~351 pJ (P-A-T), and ~291 pJ/~303 pJ (P-M-A-T) of the other devices.

Fig. 4 shows the P-A-M-T device area dependence of forming voltage and HRS/LRS values. The statistical nature of the forming process can be translated to the increase in forming voltage with decreasing device area as observed in Fig. 4**a** [34]. Furthermore, no strong dependence was observed in HRS/LRS values (Fig. 4**b**) which would indicate localised filamentary conduction [35,36].

Table 1 displays the electrical performance of various functional ReRAM stack configurations. The P-A-M-T device in this work exhibits comparable electrical performance in all aspects. Furthermore, the device was able to outperform most configurations in terms of energy consumption and retention based on the measurement conditions. In relation to these results, the P-A-M-T stack is proposed to be beneficial for low-power operations owing to the lower operating current. Furthermore, the smaller variation and larger ON/OFF resistance ratio would improve the sensing margin when incorporated into a circuit. Therefore, this balance between low operating power and small variation would be ideal for low-power NVM applications. Given these observations, the combination of higher HRS/LRS values, smaller HRS variation, and lower reset voltages could suggest conductive filament confinement and a controlled switching location at the Al_2O_3 region [23]. Thus, the conduction mechanisms of the stacks were investigated to provide further insights into these results.

With reference to the reported work on MgO-based ReRAM with similar stack configurations, the dominant conduction mechanism should be expected to follow the bulk-limited SCLC for the P-M-T stack [9,15]. To investigate this conduction mechanism, the I-V curve was plotted using a log–log scale for the positive voltage sweep region shown in Fig. 5**a**. In the HRS sweep (lower half), the I-V exhibits an Ohmic conduction at the start with $I \propto V$ (slope ~1). Increasing the voltage further results in the transition from Ohmic conduction to traps-filled limited conduction with $I \propto V^2$ (slope ~2). After switching to the LRS (upper half), dominant SCLC can still be observed during the sweep back which is in good agreement that the P-M-T stack follows SCLC [47]. Interestingly, the P-M-A-T stack also follows SCLC as seen in Fig. 5**a**. Conversely, P-A-M-T does not follow SCLC but the electrode-limited SE instead (Fig. 5**b**). Since the main difference between these three stacks is the stacking order of the device, this suggests that the dominant conduction mechanism depends on the interface between the Pt BE and SL (Pt/Al_2O_3 or Pt/MgO).

To investigate the SE further, *in-situ* temperature I-V characterization was performed on the P-A-M-T ReRAM device to observe the temperature dependence of SE that can be expressed in Eq. (2) [48]:

$$J_{SE} = A^* T^2 \exp\left[\frac{-q(\phi_B - \sqrt{qE/4\pi\varepsilon_r\varepsilon_0})}{k_B T}\right] \quad (2)$$

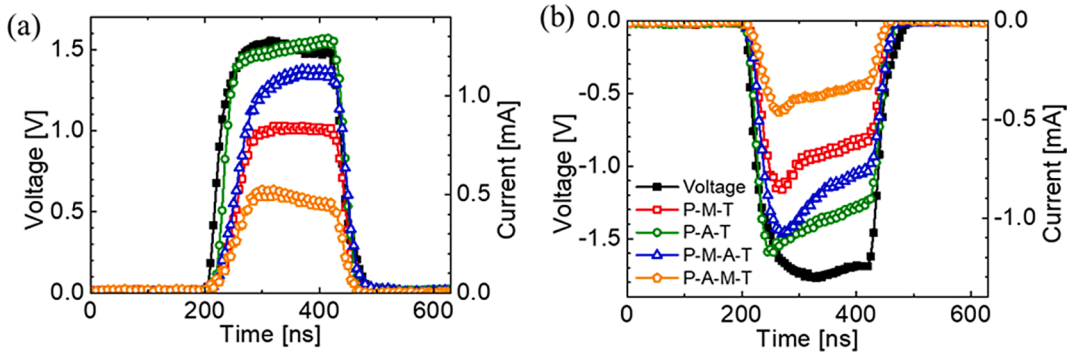

Fig. 3. Transient current response of 200 ns pulse width with rise/fall time of 20 ns on P-M-T, P-A-T, P-M-A-T, and P-A-M-T devices for (a) set (V_{set} = 1.5 V) and (b) reset (V_{reset} = -1.7 V).

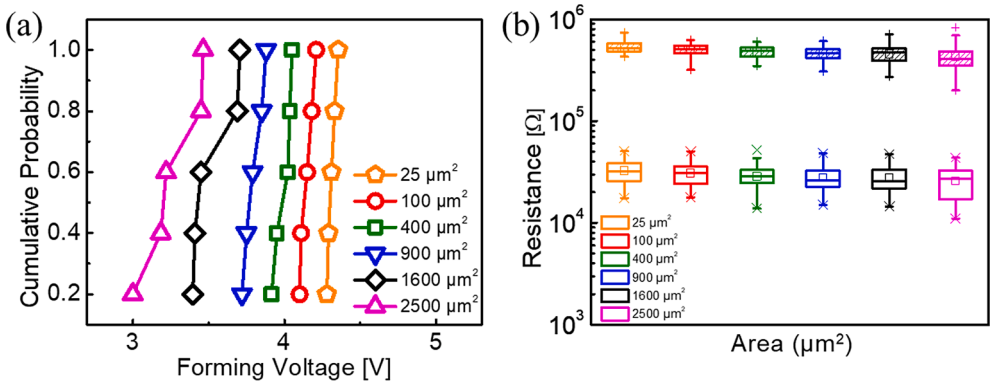

Fig. 4. Statistical distribution of the (a) forming voltage and (b) HRS/LRS values (pattern/plain) extracted at 0.2 V from 5 P-A-M-T devices × 20 cycles of each device area.

Table 1
Electrical performance of various ReRAM configurations.

ReRAM configuration	ON/OFF ratio	Energy consumption (pJ)	Endurance (cycles)	Retention (s)	Reference
$Pt/Al_2O_3/AlO_x/Cu$	$\sim10^6$	NA	>2000	$<10^4$	[37]
Ti/HfAlO/TiN	$\sim10^2$	NA	$\sim10^6$	$>10^4$	[38]
$Pt/HfO_2/TiO_x/Pt$	$\sim10^2$	NA	100	$>10^4$	[39]
$Pt/HfO_x/Ti$	~10	NA	$\sim10^3$	$\sim10^5$	[40]
$Pt/Al_2O_3/TiO_2/Pt$	$\sim10^2$	NA	~1800	NA	[41]
$Pt/HfO_2/Al_2O_3/TiN$	~15	NA	$\sim10^7$	$>10^4$	[42]
$Pt/HfO_x/AlO_x/TiN$	~5	<60.9	NA	NA	[33]
Ti/HfO_2:Al/Pt	$\sim10^2$	NA	500	$\sim10^5$	[43]
$W/Al_2O_3/HfO_2/Pt$	$\sim10^2$	NA	NA	NA	[7]
Ti/a-MgO/Pt	~8	NA	4000	$>10^4$	[9]
$TiN/HfO_2/Ti$	~10	~400	$>10^6$	NA	[44]
$TiN/S:HfO_x/ITO$	~15	$<9.08 \times 10^3$	$>10^4$	$>10^4$	[45]
TiN/HfAlO/Ti/TiN	~5	$<5 \times 10^3$	$>10^5$	$>10^5$	[46]
Pt/MgO/Ta/Ru	~10	NA	>40	$>10^4$	[15]
$Pt/Al_2O_3/MgO/Ti$	~15	<134	$>10^3$	$>10^4$	Present work

Where $A^* = \left(4\pi q m^* k_B^2/h^3\right)$, J_{SE} is the current density, T is the absolute temperature, q is the elementary charge, ϕ_B is the barrier height, E is the electric field, ε_r is the dielectric constant, ε_0 is the vacuum permittivity, k_B is Boltzmann's constant, m^* is the effective mass of electron in dielectric, and h is Planck's constant. Fig. 5**c** shows the *in-situ* temperature I-V curves in the HRS, measured from 300 K to 425 K with the voltage sweep ranging from 0.5 V to −0.5 V to prevent significant changes in resistance due to migration of oxygen ions. The asymmetry of I-V curves was an assumed consequence of the difference in metal work function between Pt and Ti. Furthermore, this asymmetry should be enhanced from the oxygen scavenging at the MgO/Ti interface and the insertion of a thin Al_2O_3 layer [12,49]. The SE can be expressed as a function of $\ln(I_{SE})$ versus $V^{1/2}$ (Fig. 5**e** and **f**), where the barrier height ϕ_B can be estimated from the intercept of a linear fit [31,50]. Therefore, the extracted Schottky barrier height at the Pt/Al_2O_3 and MgO/Ti interface is estimated to be about 0.479 eV and 0.476 eV, respectively taking the effective mass to be $m^* = 0.4m_e$ where m_e is the electron rest mass [51,52]. Additionally, the LRS temperature I-V curves exhibits a trend of increasing current with temperature (Fig. 5**d**) that could imply semiconducting behaviour instead of electronic transport in metallic Mg^{2+}. Thus, it is believed that the P-A-M-T stack demonstrates oxygen vacancies-based filamentary formation and conduction [53].

Due to the band alignment, there should be a built-in potential between the two electrodes with a lower Schottky barrier height at the MgO/Ti interface [54]. Moreover, the incorporation of Ti TE can induce sub-stoichiometric MgO_x formation at the MgO/Ti interface that might contribute further to a reduced Schottky barrier [55]. This should favour electron injection from Ti to MgO at the negative sweep compared to Pt to Al_2O_3 at the positive sweep based on the potential barrier modulation [8]. However, a further look into the asymmetrical SE I-V curves and estimated barrier heights for both Pt/Al_2O_3 and MgO/Ti interface suggests a different outcome. The experimental results (Fig. 5**c**) indicated otherwise, with a lower observable current at the negative sweep and small difference in estimated Schottky barrier height values. This slight difference in estimated values would imply a significant reduction of the barrier height at the Pt/Al_2O_3 interface. It is believed that the larger oxygen deficiency at the Pt/Al_2O_3 interface due to oxygen generation (O^{2-}) and subsequent migration towards the Ti anode during the forming/set cycle may have resulted in this variation [8,9,56]. In addition, these oxygen ions could react with Ti to form TiO_x and may have contributed to an increased barrier height at the MgO/Ti interface as well. Although the reverse can occur with migration towards Pt during the reset cycle, there would be certain limitations on the recombination (annihilation) of oxygen vacancies depending on the TiO_x barrier, dielectric-material properties, and reset voltage applied [57]. Hence, the device might be unable to return to its pristine state and switching from the LRS to HRS occurs through filament rupture at the most confined area (Al_2O_3/MgO interface) yet still leaving a larger oxygen deficiency at the Pt/Al_2O_3 interface [12].

Consistently, an asymmetry in the I-V curve with a lower current at the negative sweep was observed. Considering factors such as the formation energy of oxygen vacancies, dielectric constants, bandgaps, and oxygen scavenging effects for MgO and Al_2O_3, it suggests that the presence of an Al_2O_3 layer would have contributed to this result [12,19,25,39,58]. Consequently, asymmetries in the temperature I-V curves were observed despite the small difference in barrier heights between Pt/Al_2O_3 and MgO/Ti. These can be further exemplified in Fig. 5**g**, showing the P-A-M-T pristine device characteristics at the non-annealed (NA) and after-annealing state of 625 K and 725 K. The pristine NA device clearly exhibits the expected asymmetry with a higher negative sweep current. However, the I-V curve trend towards the results shown in Fig. 5**c** as the annealing temperature increases. This demonstrates the behaviour of thermally generated defects and enhanced drift of oxygen ions in the P-A-M-T stack that gives rise to a similar scenario as the applied voltage switching behaviour.

The inset of Fig. 5**c** illustrates schematic P-A-M-T band diagrams in

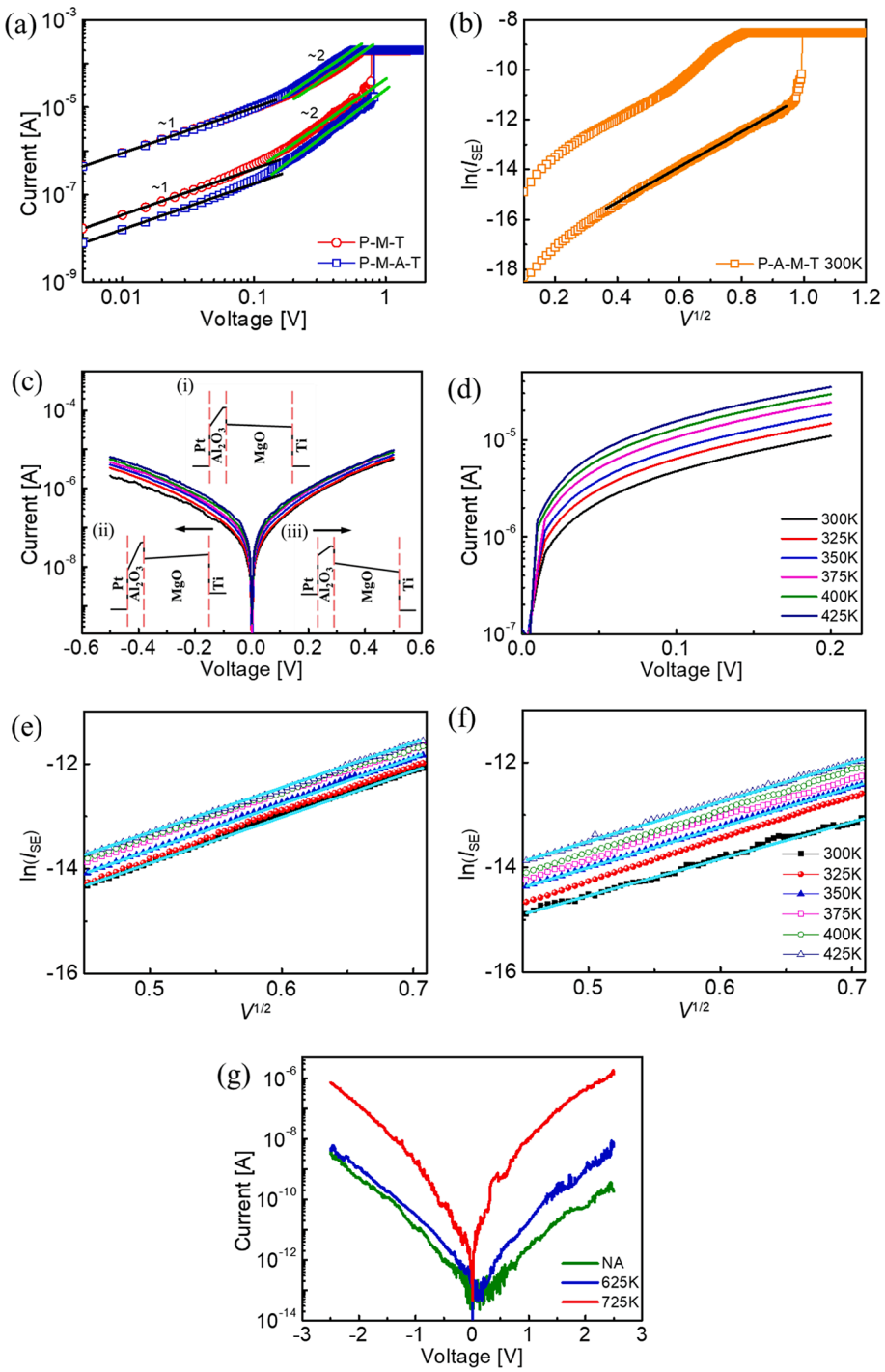

Fig. 5. (a) Fitted I-V characteristics of the P-M-T and P-M-A-T device in log–log scale demonstrating space-charge-limited conduction, starting with Ohmic conduction (slope ~1) before transitioning to traps-filled limited conduction (slope ~2). (b) Schottky emission fitting of $\ln(I_{SE})$ *vs* $V^{1/2}$ of the P-A-M-T device. I-V characteristics of the P-A-M-T device at temperatures varying from 300 K to 425 K in (c) HRS and (d) LRS. Inset shows the band diagrams of the device in HRS at no applied (i), negative applied (ii), and positive applied voltage (iii) on the Ti TE. Schottky emission fittings of $\ln(I_{SE})$ *vs* $V^{1/2}$ at various temperatures for the (e) positive and (f) negative sweeps. (g) I-V characteristics of the pristine P-A-M-T device at non-annealed (NA), and after annealing at 625 K and 725 K.

the HRS at different biases. Based on the estimated values, HRS without bias shows a slight difference in barrier heights between Pt/Al_2O_3 and MgO/Ti caused by the modulation from defects [56]. However, this difference should be less significant compared to the Al_2O_3/MgO potential barrier. Consequently, electrons injected from Ti to Pt first experience this barrier when a negative voltage is applied that will eventually overcome with sufficient voltage, leading to current being limited by the Schottky barrier at the MgO/Ti interface. On the other hand, electrons injected from Pt to Ti would experience a lower effective potential depending on the modulation by the applied positive voltage. Furthermore, Al_2O_3 should exhibit a greater amount of band bending than MgO with the same applied voltage which allows for more effective potential modulation at the positive sweep, thus resulting in a larger observable current [58].

For further clarity on the switching mechanism and chemical composition, XPS depth profile analyses were performed on the P-A-M-T and P-M-T samples in LRS. Devices of 200 × 200 μm^2 were fabricated, and an XPS measurement diameter of 110 μm was utilized. Additionally, to obtain distinctive layers for analysis, the Al_2O_3 and MgO layers have been increased proportionally to 3 nm and 12 nm, respectively. The median forming voltage and HRS/LRS for P-A-M-T were ~5.33 V and ~858 kΩ/~11 kΩ, respectively. On the other hand, the P-M-T device had a median forming voltage of ~3.98 V and HRS/LRS values of ~731 kΩ/~8 kΩ. Fig. 6**a** shows the Mg 1 s core level spectrum in the bulk MgO SL with a peak binding energy of ~1303.8 eV, while the O 1 s spectra may be deconvoluted into two peaks as shown in Fig. 6**c - f** [59,60]. The

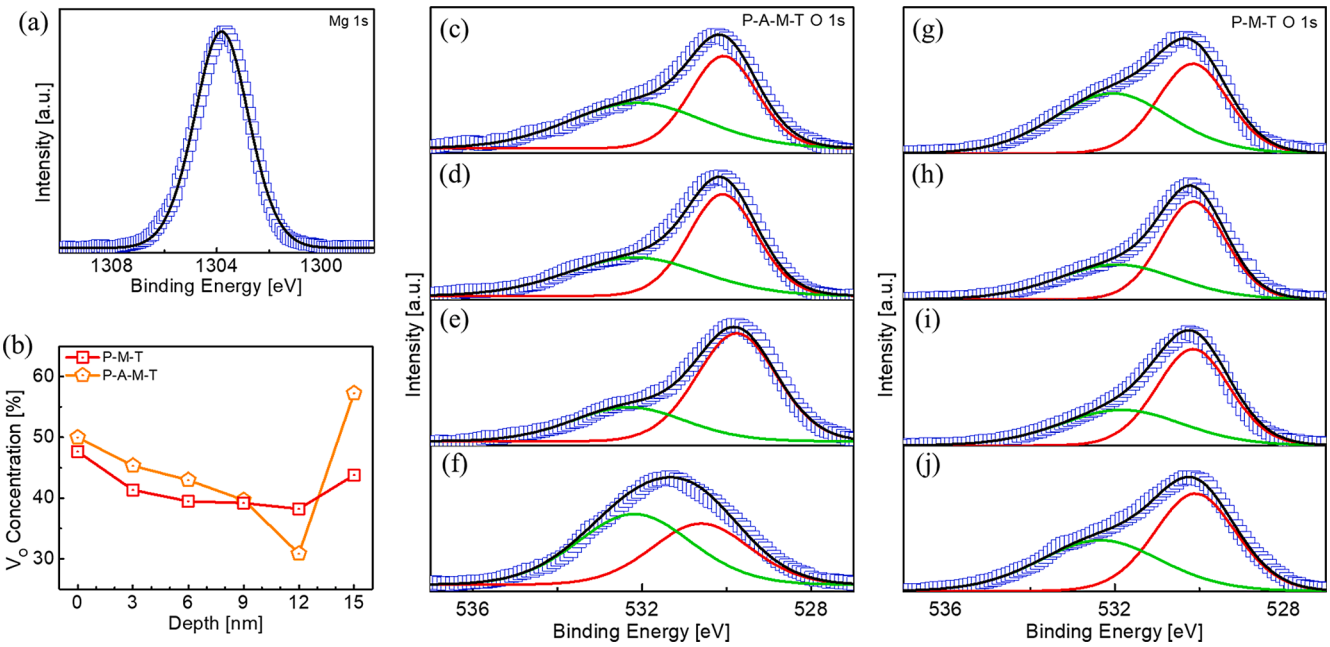

Fig. 6. (a) XPS spectrum of the P-A-M-T device in LRS for Mg 1 s. O 1 s spectra at the (c) MgO/Ti, (d) bulk MgO, (e) Al_2O_3/MgO, and (f) Pt/Al_2O_3 interfaces. O 1 s spectra from the single-layer P-M-T device at the (g) MgO/Ti, (h, i) bulk MgO, and Pt/MgO interfaces. (b) Oxygen vacancy (V_O) concentration at varying depths of the SL starting from 0 nm at the MgO/Ti interface to 15 nm at the Pt/Al_2O_3 interface or Pt/MgO interface.

lower binding energy at ~530.1 eV corresponds to lattice oxygen ions (Mg-O and Al-O bonds), whereas the higher binding energy at ~532.2 eV is ascribed to the oxygen vacancies in the SL [61,62]. The estimated proportion of each peak indicates the percentage of oxygen vacancies with 49.98 % at the MgO/Ti interface (Fig. 6**c**). The percentage decreases to 42.97 % and 30.83 % in bulk MgO (Fig. 6**d**) and at the Al_2O_3/MgO interface (Fig. 6**e**), respectively. Finally, an increase to 57.27 % was observed at the Pt/Al_2O_3 interface (Fig. 6**f**). From the single-layer XPS depth profile analysis of P-M-T, there was a lack of filamentary confinement that was observed in the P-A-M-T device. In addition, the P-M-T device had an overall lower V_o concentration throughout the SL. Thus, it is believed that the improvements in electrical properties were a consequence of the filamentary constriction at the MgO/Al_2O_3 interface. Fig. 6**b** highlights the oxygen vacancy concentration based on the XPS

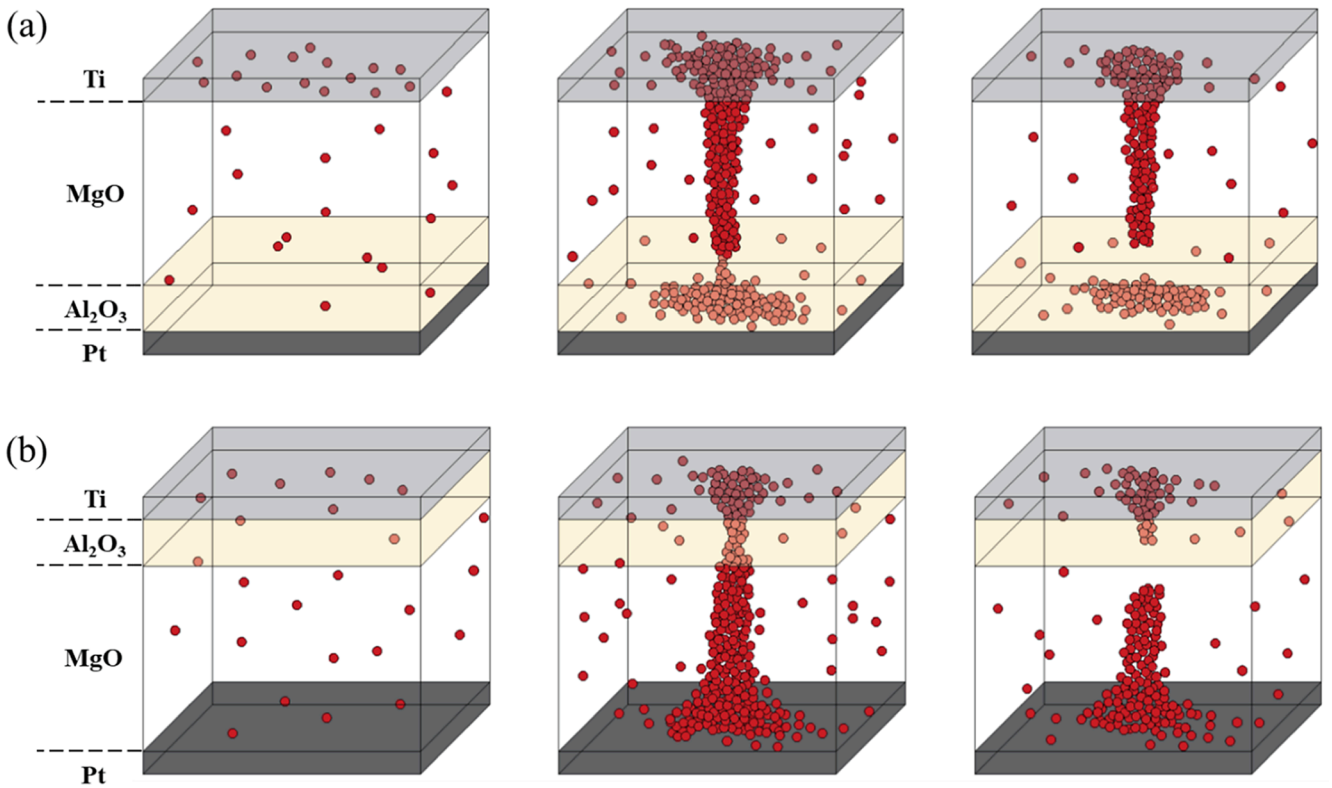

Fig. 7. Schematic diagrams of the pristine, and subsequent switching descriptions of oxygen vacancies (defects) in the (a) P-A-M-T and (b) P-M-A-T device.

depth profile analysis of the P-A-M-T and P-M-T device in LRS starting from the MgO/Ti to Pt/Al_2O_3 or Pt/MgO interface.

Based on the results in this work, the resistive switching behaviour of the P-A-M-T stack can be illustrated in Fig. 7**a**. The device starts with the pristine state that has a Ti-induced sub-stoichiometric MgO_x region and random as-deposited defects throughout the SL [63]. During the forming cycle, defect generation and subsequent O^{2-} migration towards the Ti anode leads to a gradual filament formation. Hence, the generated defects are believed to accumulate at the Pt/Al_2O_3 interface that in turn lowers the Schottky barrier height. However, the difficulty in locally generated oxygen vacancy and interstitial defects of Al_2O_3 compared to MgO should result in a narrow filament at the Al_2O_3/MgO interface towards the Al_2O_3 layer [23]. This increases the probability of recombination and filament rupture taking place in that region owing to a lower defect density and stronger chemical affinity, which can be correlated to the lower reset voltage of P-A-M-T (-0.68 V) as compared to P-M-T (-0.73 V). Moreover, the recovery of the Al_2O_3 layer near the Al_2O_3/MgO interface limits additional O^{2-} migration towards the Pt BE due to the oxygen barrier property of the dielectric. Thus, significant defects will remain at the Pt/Al_2O_3 interface in the HRS but can vary according to the reset voltage applied. The noticeable improvements in terms of HRS/LRS values, HRS variation, and reset voltages as demonstrated are achieved through the resistive switching behaviour of the P-A-M-T stack. In addition, the increase in set voltage of P-A-M-T (0.97 V) as compared to P-M-T (0.86 V) could suggest the difficulty of subsequent filament formations in the Al_2O_3 layer.

To the contrary, the resistive switching behaviour of the P-M-A-T stack (Fig. 7**b**) exemplifies the large switching variability observed in the experimental results. With the change in stacking order, it is assumed that the oxygen scavenging effect and defect accumulation would be suppressed at the Al_2O_3/Ti interface [7]. Moreover, the oxygen barrier property limits O^{2-} migration into the Al_2O_3 layer during the forming/set cycle. Thus, filament rupture is expected to take place at the MgO/Al_2O_3 interface towards the MgO layer. Consequently, there would be a lack of overall control on the recombination of oxygen vacancies in the wider filament during the reset process which may further affect the filament in the bulk of the MgO layer. This should have contributed to fluctuations in the subsequent set/reset processes that translates to the large HRS/LRS variation observed in the experimental results.

4. Conclusions

In summary, the resistive switching characteristics of MgO- and Al_2O_3-based ReRAM devices have been investigated. The improvements towards lower power operations (50.6 % reduction) and smaller variations were attributed to the incorporation of the Al_2O_3 layer. The Al_2O_3 layer allows for a more constricted and controllable filament formation and rupture due to its dielectric-material properties. However, investigations have shown that these improvements largely depend on the stacking order of the SL, with P-A-M-T exhibiting these favourable properties. In addition, the dominant conduction mechanisms of SE for P-A-M-T, SCLC for P-M-T and P-M-A-T have been explained and verified. This study provides insights towards the development of MgO-based ReRAM devices for low-power non-volatile memory applications.

CRediT authorship contribution statement

Samuel Chen Wai Chow: Conceptualization, Methodology, Data curation, Investigation, Writing – original draft. **Putu Andhita Dananjaya:** Conceptualization, Visualization, Writing – review & editing. **Jia Min Ang:** Software. **Desmond Jia Jun Loy:** Writing – review & editing. **Jia Rui Thong:** Methodology. **Siew Wei Hoo:** Methodology. **Eng Huat Toh:** Supervision, Writing – review & editing. **Wen Siang Lew:** Supervision, Writing – review & editing.

Declaration of Competing Interest

The authors declare that they have no known competing financial interests or personal relationships that could have appeared to influence the work reported in this paper.

Data availability

Data will be made available on request.

Acknowledgement

This work was supported by RIE2020 A*STAR, Singapore AME IAF-ICP (Grant No. I1801E0030); and EDB-IPP (Grant No. RCA2019-1376).

References

[1] A. Chen, A review of emerging non-volatile memory (NVM) technologies and applications, Solid-State Electron. 125 (2016) 25–38.
[2] S. Yu, Resistive Random Access Memory (RRAM) (2016).
[3] L. Zhu, J. Zhou, Z. Guo, Z. Sun, An overview of materials issues in resistive random access memory, J. Materiomics 1 (4) (2015) 285–295.
[4] B.J. Choi, A.C. Torrezan, K.J. Norris, F. Miao, J.P. Strachan, M.-X. Zhang, D.A. A. Ohlberg, N.P. Kobayashi, J.J. Yang, R.S. Williams, Electrical performance and scalability of Pt dispersed SiO_2 nanometallic resistance switch, Nano Lett. 13 (7) (2013) 3213–3217.
[5] C.H. Lien, Y.S. Chen, H.Y. Lee, P.S. Chen, F.T. Chen, M.J. Tsai, The highly scalable and reliable hafnium oxide ReRAM and its future challenges, in: IEEE International Conference on Solid-State and Integrated Circuit Technology, 2010, pp. 1084–1087.
[6] F. Zahoor, T.Z. Azni Zulkifli, F.A. Khanday, Resistive Random Access Memory (RRAM): an overview of materials, switching mechanism, performance, multilevel cell (mlc) storage, modeling, and applications, Nanoscale Res. Lett. 15 (2020).
[7] E. Shahrabi, C. Giovinazzo, J. Sandrini, Y. Leblebici, The key impact of incorporated Al_2O_3 barrier layer on W-based ReRAM switching performance, PRIME 2018 - 14th Conference on Ph.D. Research in Microelectronics and Electronics. (2018) 69–72.
[8] J.J. Huang, C.W. Kuo, W.C. Chang, T.H. Hou, Transition of stable rectification to resistive-switching in Ti/TiO_2/Pt oxide diode, Appl. Phys. Lett. 96 (2010) 23–26.
[9] J. Guo, S. Ren, L. Wu, X. Kang, W. Chen, X. Zhao, Low-power, high-uniform, and forming-free resistive memory based on Mg-deficient amorphous MgO film with rough surface, Appl. Surf. Sci. 434 (2018) 1074–1078.
[10] S. Park, K. Cho, J. Jung, S. Kim, Annealing effect of Al_2O_3 tunnel barriers in HfO_2-based ReRAM devices on nonlinear resistive switching characteristics, J. Nanosci. Nanotechnol. 15 (10) (2015) 7569–7572.
[11] K.Y. Cheong, I.A. Tayeb, F. Zhao, J.M. Abdullah, Review on resistive switching mechanisms of bio-organic thin film for non-volatile memory application, Nanotechnology Reviews. 10 (2021) 680–709.
[12] L. Goux, A. Fantini, B. Govoreanu, G. Kar, S. Clima, Y.-Y. Chen, R. Degraeve, D. J. Wouters, G. Pourtois, M. Jurczak, Asymmetry and switching phenomenology in TiN\(Al_2O 3)\$Hf_O$2\Hf systems, ECS Solid State Letters. 1 (4) (2012) P63–P65.
[13] J.Y. Chen, Y.C. Lau, J.M.D. Coey, M. Li, J.P. Wang, High performance MgO-barrier magnetic tunnel junctions for flexible and wearable spintronic applications, Sci. Rep. 7 (2017) 1–7.
[14] J.M. Teixeira, J. Ventura, R. Fermento, J.P. Araujo, J.B. Sousa, P. Wisniowski, P. P. Freitas, Electroforming, magnetic and resistive switching in MgO-based tunnel junctions, J. Phys. D Appl. Phys. 42 (2009).
[15] L.M. Guerra, C. Dias, J. Pereira, H. Lv, S. Cardoso, P.P. Freitas, J. Ventura, Unipolar nonvolatile resistive switching in Pt/MgO/Ta/Ru structures deposited by magnetron sputtering, J. Nanosci. Nanotechnol. 17 (1) (2017) 564–567.
[16] W. Lu, W. Chen, Y. Li, R. Jha, Self current limiting MgO ReRAM devices for low-power non-volatile memory applications, IEEE J. Emerging Sel. Top. Circuits Syst. 6 (2) (2016) 163–170.
[17] C. Dias, L.M. Guerra, B.D. Bordalo, H. Lv, A.M. Ferraria, A.M. Botelho do Rego, S. Cardoso, P.P. Freitas, J. Ventura, Voltage-polarity dependent multi-mode resistive switching on sputtered MgO nanostructures, PCCP 19 (17) (2017) 10898–10904.
[18] L. Yan, C.M. Lopez, R.P. Shrestha, E.A. Irene, A.A. Suvorova, M. Saunders, Magnesium oxide as a candidate high- κ gate dielectric, Appl. Phys. Lett. 88 (2006) 6–9.
[19] B. Kumar, B.K. Kaushik, Y.S. Negi, Perspectives and challenges for organic thin film transistors: Materials, devices, processes and applications, J. Mater. Sci.: Mater. Electron. 25 (2014) 1–30.
[20] A. Posadas, F.J. Walker, C.H. Ahn, T.L. Goodrich, Z. Cai, K.S. Ziemer, Epitaxial MgO as an alternative gate dielectric for SiC transistor applications, Appl. Phys. Lett. 92 (2008) 10–13.
[21] Y. Kaneko, N. Mikoshiba, T. Yamashita, Preparation of MgO thin films by RF magnetron sputtering, Jpn. J. Appl. Phys. 30 (Part 1, No. 5) (1991) 1091–1092.
[22] S.L. Fang, W.H. Liu, X. Li, X.L. Wang, L.i. Geng, M.S. Wu, X.D. Huang, C.Y. Han, Biodegradable transient resistive random-access memory based on MoO_3/MgO/MoO_3 stack, Appl. Phys. Lett. 115 (24) (2019) 244102.

[23] L. Goux, N. Raghavan, A. Fantini, R. Nigon, S. Strangio, R. Degraeve, G. Kar, Y. Y. Chen, F. De Stefano, V.V. Afanas'ev, M. Jurczak, On the bipolar resistive-switching characteristics of Al_2O_3- and HfO_2-based memory cells operated in the soft-breakdown regime, J. Appl. Phys. 116 (13) (2014) 134502.

[24] W. Liu, L. Gao, K. Xu, F. Ma, Impact of ultrathin Al_2O_3 interlayers on resistive switching in TiO_x thin films deposited by atomic layer deposition, Journal of Vacuum Science & Technology B, Nanotechnology and Microelectronics: Materials, Processing, Measurement, and Phenomena. 35 (2017), 041001.

[25] J. Robertson, Band offsets of wide-band-gap oxides and implications for future electronic devices, Journal of Vacuum Science & Technology B: Microelectronics and Nanometer Structures. 18 (3) (2000) 1785.

[26] W. Song, W. Wang, H.K. Lee, M. Li, V.Y.Q. Zhuo, Z. Chen, K.J. Chui, J.C. Liu, I. T. Wang, Y. Zhu, N. Singh, Analog switching characteristics in TiW/Al_2O_3/Ta_2O_5/Ta RRAM devices, Appl. Phys. Lett. 115 (2019) 1–5.

[27] C. Mahata, M. Kang, S. Kim, Multi-level analog resistive switching characteristics in tri-layer HfO_2/Al_2O3/HfO_2 based memristor on ITO electrode, Nanomaterials. 10 (2020) 1–12.

[28] M. Lanza, R. Waser, D. Ielmini, J.J. Yang, L. Goux, J. Suñe, A.J. Kenyon, A. Mehonic, S. Spiga, V. Rana, S. Wiefels, S. Menzel, I. Valov, M.A. Villena, E. Miranda, X.u. Jing, F. Campabadal, M.B. Gonzalez, F. Aguirre, F. Palumbo, K. Zhu, J.B. Roldan, F.M. Puglisi, L. Larcher, T.-H. Hou, T. Prodromakis, Y. Yang, P. Huang, T. Wan, Y. Chai, K.L. Pey, N. Raghavan, S. Dueñas, T. Wang, Q. Xia, S. Pazos, Standards for the characterization of endurance in resistive switching devices, ACS Nano 15 (11) (2021) 17214–17231.

[29] M.-J. Lee, C.B. Lee, D. Lee, S.R. Lee, M. Chang, J.H. Hur, Y.-B. Kim, C.-J. Kim, D. H. Seo, S. Seo, U.-I. Chung, I.-K. Yoo, K. Kim, A fast, high-endurance and scalable non-volatile memory device made from asymmetric Ta_2O_{5-x}/TaO_{2-x} bilayer structures, Nat. Mater. 10 (8) (2011) 625–630.

[30] J. Park, M. Jo, E.M. Bourim, J. Yoon, D.J. Seong, J. Lee, W. Lee, H. Hwang, Investigation of state stability of low-resistance state in resistive memory, IEEE Electron Device Lett. 31 (2010) 485–487.

[31] D.J.J. Loy, P.A. Dananjaya, X.L. Hong, D.P. Shum, W.S. Lew, Conduction mechanisms on high retention annealed MgO-based resistive switching memory devices, Sci. Rep. 8 (2018) 1–9.

[32] Z. Wei, Y. Kanzawa, K. Arita, Y. Katoh, K. Kawai, S. Muraoka, S. Mitani, S. Fujii, K. Katayama, M. Iijima, T. Mikawa, T. Ninomiya, R. Miyanaga, Y. Kawashima, K. Tsuji, A. Himeno, T. Okada, R. Azuma, K. Shimakawa, H. Sugaya, T. Takagi, R. Yasuhara, KHoriba, H. Kumigashira, M. Oshima, Highly reliable TaO_x ReRAM and direct evidence of redox reaction mechanism, Technical Digest - International Electron Devices Meeting, IEDM. (2008) 4–7.

[33] S. Yu, Y. Wu, H.S.P. Wong, Investigating the switching dynamics and multilevel capability of bipolar metal oxide resistive switching memory, Appl. Phys. Lett. 98 (2011) 1–4.

[34] A. Chen, Area and thickness scaling of forming voltage of resistive switching memories, IEEE Electron Device Lett. 35 (2014) 57–59.

[35] H.Y. Peng, G.P. Li, J.Y. Ye, Z.P. Wei, Z. Zhang, D.D. Wang, G.Z. Xing, T. Wu, Electrode dependence of resistive switching in Mn-doped ZnO: Filamentary versus interfacial mechanisms, Appl. Phys. Lett. 96 (2010) 2008–2011.

[36] W. Guan, S. Long, Q. Liu, M. Liu, W. Wang, Nonpolar nonvolatile resistive switching in Cu doped ZrO2, IEEE Electron Device Lett. 29 (2008) 434–437.

[37] S.K. Vishwanath, H. Woo, S. Jeon, Enhancement of resistive switching properties in Al_2O_3 bilayer-based atomic switches: Multilevel resistive switching, Nanotechnology. 29 (2018).

[38] B. Traoré, P. Blaise, E. Vianello, H. Grampeix, A. Bonnevialle, E. Jalaguier, G. Molas, S. Jeannot, L. Perniola, B. DeSalvo, Y. Nishi, Microscopic understanding of the low resistance state retention in HfO_2 and HfAlO based RRAM, Technical Digest - International Electron Devices Meeting, IEDM. (2015) 21.5.1.

[39] X. Ding, Y. Feng, P. Huang, L. Liu, J. Kang, Low-Power Resistive Switching Characteristic in HfO_2/TiO_x Bi-Layer Resistive Random-Access Memory, Nanoscale Res Lett. 14 (1) (2019).

[40] L. Wu, H. Liu, J. Lin, S. Wang, Self-compliance and high performance Pt/HfO_x/Ti RRAM achieved through annealing, Nanomaterials. 10 (3) (2020) 457.

[41] H. Jeon, J. Park, W. Jang, H. Kim, S. Ahn, K.J. Jeon, H. Seo, H. Jeon, Detection of oxygen ion drift in Pt/Al_2O_3/TiO_2/Pt RRAM using interface-free single-layer graphene electrodes, Carbon N Y. 75 (2014) 209–216.

[42] H. Luo, Y. Liang, M. Tang, G. Li, Y. Xiong, Y. Sun, Y. Liu, S. Ouyang, Y. Xiao, S. Yan, W. Zhang, Q. Chen, Z. Li, Total ionizing dose effects on resistance stability of Pt/HfO_2/Al_2O_3/TiN structure RRAM devices, Microelectron. Reliab. 106 (2020) 113592.

[43] J. Lin, S. Wang, H. Liu, Multi-level switching of al-doped HfO_2 RRAM with a single voltage amplitude set pulse, Electronics (Switzerland). 10 (2021) 1–10.

[44] G. Sassine, C. Nail, L. Tillie, D.A. Robayo, A. Levisse, C. Cagli, K. el Hajjam, J. F. Nodin, E. Vianello, M. Bernard, G. Molas, E. Nowak, Sub-pJ consumption and short latency time in RRAM arrays for high endurance applications, IEEE International Reliability Physics Symposium Proceedings. (2018-March (2018)) PMY.21–PMY.25.

[45] Z. Zhang, F. Wang, K. Hu, Y.u. She, S. Song, Z. Song, K. Zhang, Improvement of resistive switching performance in sulfur-doped HfO_x-based rram, Materials. 14 (12) (2021) 3330.

[46] E. Pérez, Ó. González Ossorio, S. Dueñas, H. Castán, H. García, C. Wenger, Programming pulse width assessment for reliable and low-energy endurance performance in al:HfO_2-based rram arrays, Electronics (Switzerland). 9 (5) (2020) 864.

[47] F.-C. Chiu, A review on conduction mechanisms in dielectric films, Adv. Mater. Sci. Eng. 2014 (2014) 1–18.

[48] F.C. Chiu, Z.H. Lin, C.W. Chang, C.C. Wang, K.F. Chuang, C.Y. Huang, J.Y.M. Lee, H.L. Hwang, Electron conduction mechanism and band diagram of sputter-deposited Al/ZrO_2/Si structure, J. Appl. Phys. 97 (2005).

[49] I. Tanaka, F. Oba, K. Tatsumi, M. Kunisu, M. Nakano, H. Adachi, Theoretical formation energy of oxygen-vacancies in oxides, Mater. Trans. 43 (7) (2002) 1426–1429.

[50] E.W. Lim, R. Ismail, Conduction mechanism of valence change resistive switching memory: A survey, Electronics (Switzerland). 4 (2015) 586–613.

[51] C.W. Miller, Z.P. Li, I.K. Schuller, R.W. Dave, J.M. Slaughter, J. Akerman, Dynamic spin-polarized resonant tunneling in magnetic tunnel junctions, Phys. Rev. Lett. 99 (2007) 1–5.

[52] Y.N. Kulchin, V.P. Dzyuba, A.V. Amosov, Exciton states of the optical electrons of Al_2O_3 nanoparticles in dielectric matrix, Pacific Science, Review. 16 (3) (2014) 170–177.

[53] T. Zhang, J. Yin, Y. Xia, W. Zhang, Z. Liu, Conduction mechanism of resistance switching in fully transparent MgO-based memory devices, J. Appl. Phys. 114 (13) (2013) 134301.

[54] V.Y.Q. Zhuo, Y. Jiang, M.H. Li, E.K. Chua, Z. Zhang, J.S. Pan, R. Zhao, L.P. Shi, T. C. Chong, J. Robertson, Band alignment between Ta_2O_5 and metals for resistive random access memory electrodes engineering, Appl. Phys. Lett. 102 (2013) 1–6.

[55] A. Padovani, L. Larcher, P. Padovani, C. Cagli, B. de Salvo, Understanding the role of the Ti metal electrode on the forming of HfO_2-based RRAMs, 2012 4th IEEE International Memory Workshop, IMW 2012 (1) (2012).

[56] L. Pantisano, V.V. Afanas'ev, S. Cimino, C. Adelmann, L. Goux, Y.Y. Chen, J. A. Kittl, D. Wouters, M. Jurczak, Towards barrier height modulation in HfO_2/TiN by oxygen scavenging - Dielectric defects or metal induced gap states? Microelectron. Eng. 88 (7) (2011) 1251–1254.

[57] S. Yu, H.-S. Wong, A phenomenological model for the reset mechanism of metal oxide RRAM, IEEE Electron Device Lett. 31 (12) (2010) 1455–1457.

[58] R.G. Southwick, A. Sup, A. Jain, W.B. Knowlton, An interactive simulation tool for complex multilayer dielectric devices, IEEE Trans. Device Mater. Reliab. 11 (2) (2011) 236–243.

[59] J. Li, Y. Jiang, Y. Li, D. Yang, Y. Xu, M. Yan, Origin of room temperature ferromagnetism in MgO films, Appl. Phys. Lett. 102 (2013) 1–5.

[60] Y. Wan, C. Samundsett, J. Bullock, M. Hettick, T. Allen, D.i. Yan, J. Peng, Y. Wu, J. Cui, A. Javey, A. Cuevas, Conductive and stable magnesium oxide electron-selective contacts for efficient silicon solar cells, Adv. Energy Mater. 7 (5) (2017) 1601863.

[61] L.-G. Wang, X.u. Qian, Y.-Q. Cao, Z.-Y. Cao, G.-Y. Fang, A.-D. Li, D.i. Wu, Excellent resistive switching properties of atomic layer-deposited Al_2O_3/HfO_2/Al_2O_3 trilayer structures for non-volatile memory applications, Nanoscale Res. Lett. 10 (1) (2015).

[62] J. Raja, C.P.T. Nguyen, C. Lee, N. Balaji, S. Chatterjee, K. Jang, H. Kim, J. Yi, Improved data retention of InSnZnO nonvolatile memory by H_2O_2 treated Al_2O_3 tunneling layer: A cost-effective method, IEEE Electron Device Lett. 37 (10) (2016) 1272–1275.

[63] H.R.J. Cox, M. Buckwell, W.H. Ng, D.J. Mannion, A. Mehonic, P.R. Shearing, S. Fearn, A.J. Kenyon, A nanoscale analysis method to reveal oxygen exchange between environment, oxide, and electrodes in ReRAM devices, APL Mater. 9 (11) (2021) 111109.